SCIENTIFIC REPORTS
natureresearch

Check for updates

OPEN

Theoretical and experimental investigation of Xenotime-type rare earth phosphate REPO$_4$, (RE = Lu, Yb, Er, Y and Sc) for potential environmental barrier coating applications

Jing Han, Yanfei Wang✉, Rongjun Liu & Fan Wan

The mechanical and thermophysical properties of Xenotime-type REPO$_4$ (RE = Lu, Yb, Er, Y and Sc) have been theoretically and experimentally investigated for a potential environmental barrier coating (EBC) topcoat application. The results show that the current studied REPO$_4$ exhibits a quasi-ductile property, suggesting a potential long life expectancy of its made coatings. Further, from the study of underlying parameters governing thermophysical properties of a ceramic, low thermal expansion coefficients (TECs) and low thermal conductivities cannot be achieved simultaneously, due to mutual exclusive nature of above two parameters. REPO$_4$ has been unveiled to have rather small TECs, attributing partly to its weak lattice anharmonicity, and is thus well-matched with silicon carbide based ceramic matrix composites. Last, the current investigated REPO$_4$ exhibits very good high-temperature water vapor corrosion resistance, excellent calcium-magnesium aluminosilicates (CMAS) resistance as well as excellent chemical compatibility with silicon bond coats at elevated temperatures. Therefore, the Xenotime-type rare earth phosphates are a promising EBC topcoat material.

In order to achieve a higher thermal efficiency, according to Carnot Cycle, there is endless driving force to increase the inlet temperature of advanced gas turbines[1–3]. With the increase of operation temperatures, it of course imposes more thermal loads to hot-section components, and hence makes the thermal environment more deteriorate and thus severely challenges corresponding materials. Unfortunately, the conventional nickel based superalloys cannot survive these demanding environments, and silicon carbide based ceramic matrix composites (CMCs) are a promising candidate to replace those superalloys due to a combination of superior properties such as: superior high-temperature mechanical properties, excellent oxidation/thermal shock resistances, high reliability and damage tolerance, low densities, as well as their excellent high temperature stability, which is capable of surviving temperatures higher than 1,400 °C, a temperature well above superalloy's upper limit[4]. However, one fatal drawback of silicon carbide based CMCs as a gas turbine hot-section component is that they tend to react with high-temperature water vapor, a byproduct of fuel combustion, which results in a rapid recession of CMCs and thus cannot satisfy the reliability and durability criteria for aero-engine application. In this sense, the prevention and protection of silicon carbide based CMCs in high-temperature combustion gases that are both oxidative and rich in water vapor is the core and bottleneck technology[5–7].

In order to address above problems, there are mainly two strategies. One is to develop a more oxidation and water–vapor resistant CMCs, such as to employ an oxidation and water vapor-resistant compounds to modify both interphase[8,9] and matrix[10,11] of CMCs. This work is still under way. The other strategy is more direct and

Science and Technology On Advanced Ceramic Fibers and Composites Laboratory, College of Aerospace Science and Engineering, National University of Defense Technology, Changsha 410073, P. R. China. ✉email: wangyanfei@nudt.edu.cn

simple, that is to employ a so-called environmental barrier coating, EBC, to physically isolate the harmful combustion gases and CMC components[4–7]. Despite of different functions, EBC is rather similar to thermal barrier coating (TBC), the main function of latter is to provide a thermal insulation so as to increase working temperature of gas turbines. Similar to TBC, EBC has at least two layers, which are bond coat and top coat[5]. The main function of EBC bond coat is to provide sufficient adhesion and oxidation resistance, and silicon is the common choice in the state-of-art[12–14]. The problem of Si bond coat is poor oxidation resistance and limited temperature capability restrained by its melting point, which is around 1,410 °C. To address these issues, a hafnium oxide (HfO_2) modified Si bond coat is proposed to improve its oxidation resistance by forming a $HfSiO_4$ phase[12–14]. Meanwhile, a rare earth silicide compound has been proposed as a high-temperature capable bond coat by a U.S. patent[15].

On the other hand, as EBC top coats directly contacts with combustion gases, their main function is to improve environmental durability. That is to say, EBC top coats have to be both water vapor and calciummagnesium aluminosilicates (CMAS) resistant[16,17]. In addition, as EBC is a prime reliant coating, which indicates its failure could perhaps lead to a catastrophic consequence, the reliability and durability are of primary concern[17]. To ensure long durability and good reliability, a low stress level of EBC coating system is mandatory[17]. In this regard, the thermal expansion coefficient (TEC) matching between top coats and substrate CMCs is a top priority. A larger TEC of top coats compared to CMC substrates tend to generate tensile stress, which drives to form mud cracks during thermal cycling[18]. These mud cracks allow hot corrosive combustion gases directly attack bond coats or CMC substrates, leading to their rapid failure[18]. Besides, a good phase stability, low elastic modulus and good sintering resistance of top coats are all favored to produce low stress levels and thus a good lifespan of relevant EBCs[17].

To date, there are three generations of EBC top coats developed, which are the first generation mullite (i.e. $Al_2O_3 \cdot SiO_2$ oxide mixtures)[2], the second generation BSAS (i.e. $BaO \cdot SrO \cdot Al_2O_3 \cdot SiO_2$ oxide mixtures)[2,19,20] and the third generation rare earth disilicates ($RE_2Si_2O_7$) or monsilicates (RE_2SiO_5)[2,19]. If we closely examine these three generations of EBC topcoats, it is easy to find that they are all silicon containing compounds. In addition, despite of different chemical compositions of all these three-generation EBC topcoats, they in fact degrade for the same reason, that is, the volatility of silicon due to water vapor attack, attributing to the weak bonding of Si–O bonds[21]. The implication of this is that, if it is possible to develop a compound without silicon, it perhaps can find a more water vapor resistant EBC top coat. Following this clue, in the current study, we select a rare earth phosphate, $REPO_4$, as a potential EBC top coat material. The fact is that P-O bonds in $REPO_4$ are much stronger than those of Si–O bonds in the above compounds. Besides, $REPO_4$ has already proposed as a potential TBC topcoat as suggested by Feng et al.[22] and Wang et al.[23], indicating they possess a good high temperature phase stability, and even more encouragingly, a very good CMAS resistant property[23]. Note that in[22,23] larger RE cations are employed, forming a monoclinic (or Monazite-type) phase, which has a larger thermal expansion coefficient (from $8-10 \times 10^{-6} K^{-1}$)[22] and is thus not appropriate for EBC application. By contrast, those RE phosphates with smaller RE cations, such as YPO_4[24] and $LuPO_4$[21], tend to form a tetragonal (or Xenotime-type) phase with much smaller TEC values, for instance, $5.9 \times 10^{-6} K^{-1}$ for $LuPO_4$[21]. As a result, they are promising EBC topcoats[21,24].

In the current study, we have systematically investigated the mechanical and thermophysical properties of a Xenotime-type $REPO_4$ with smaller RE cations, i.e. RE including Lu, Yb, Er, Y and Sc, for potential EBC topcoat applications. First, we employ first-principle calculations to predict elastic constants of $REPO_4$ (RE = Lu, Yb, Er, Y and Sc), on the basis of which the mechanical properties can then be calculated. Second, the thermophysical properties (i.e. thermal expansion coefficients and thermal diffusivities) of $REPO_4$ can be measured. From the discussion of underlying parameters dictating those thermophysical properties, it is for the first time unveiled that a low thermal expansion coefficient and a low thermal conductivity are mutually exclusive and thus cannot be achieved simultaneously. Lastly, the water vapor corrosion resistance and chemical compatibility of $REPO_4$ with Si bond coat are experimentally studied to justify them as a potential EBC topcoat.

Methodology

Theoretical calculation methods. The elastic constants of $REPO_4$ (RE = Lu, Yb, Er, Y and Sc) are theoretically predicted based on first principles calculations. The calculations are carried out employing the CASTEP code[25]. The plane wave basis is used under periodic boundary conditions. The kinetic energy cutoff is set to 500 eV for expanding Bloch waves in the reciprocal space. For the energy integrations, a discretized $5 \times 5 \times 5$ k sampling grid is applied in the first irreducible Brillouin zone based on Monkhorst–Pack method[26]. For the exchange correlation energy, polarized generalized gradient approximation (GGA) is used[27]. The crystal structures are fully optimized by independently modifying lattice parameters and internal atomic coordinates. The Broyden–Fletcher–Goldfarb–Shanno (BFGS) minimization scheme29 has been employed to minimize the total energy and interatomic forces. For the pseudo-atoms, the ultra-soft type pseudopotentials are applied for RE, P, and O atoms to account for the electrostatic interactions between valence electrons and ionic cores. The criteria for convergence in geometry optimization are selected as follows: the difference in total energy within 1×10^{-6} eV/atom, the ionic Hellmann–Feynman forces within 0.002 eV/Å, the maximum stress within 0.01 GPa and the maximum ionic displacement within 1×10^{-4} Å.

Material preparation and characterization. The thermophysical properties (i.e. thermal diffusivity, thermal expansion coefficient) of $REPO_4$ are experimentally measured from the sintered $REPO_4$ ceramic bulks. The starting $REPO_4$ (RE = Lu, Yb, Er, Y and Sc) powders and Yb_2SiO_5, $Yb_2Si_2O_7$ powders (which are used as a reference to compare water vapor corrosion rates) are all 99.9% pure, purchased from the Kai-Star Electro-Optic Materials, Wuxi, China. The powders were cold isostatic pressed at 50 MPa into disk-shaped (12.7 mm in
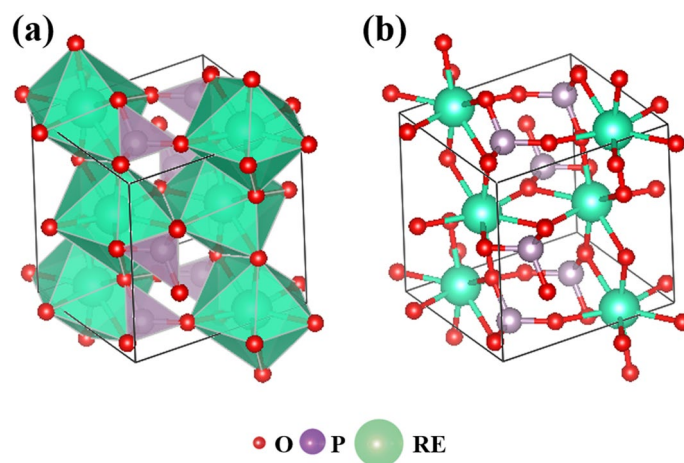
Figure 1. Crystal structure of rare earth phosphate REPO₄.

diameter × 2 mm high) and bar-shaped (5 mm × 5 mm × 25 mm) green compacts. The green compacts were then sintered at 1,500 °C for 20 h in air.

The densities of bulks were measured by Archimedes' method in distilled water. The phases were examined by X-ray diffraction (XRD, Bruker D8 Advanced, Cu Kα radiation). The thermal diffusivity is measured by means of the laser flash technique, using thermal constant measurement equipment (NETZSCH LFA 427, Bavaria, Germany). The thermal conductivity k (in W/m•K) was calculated from the equation:

$$k = c_p D \rho \tag{1}$$

where c_p is the specific heat (in J/kg•K), D the thermal diffusivity (in cm²/s), and ρ the density (in g/cm³). The specific heat capacitance is calculated according to the Neumann–Kopp rule[28] by employing standard c_p values extracted from[29]. Thermal expansion coefficients (TECs) were obtained from temperature-dependent changes in the length of the specimens from room temperature to 1,350 °C in air as determined using a vertical high-temperature optical dilatometer (ODHT, Modena, Italy).

The water vapor corrosion behaviors of sintered ceramic bulks were investigated in 50% H₂O/50% O₂ water vapor flowing at a rate of 0.30 cm/s with an atmospheric pressure at 1,500 °C for 80 h. The water vapor was introduced to an alumina tube by O₂ carrier gas bubbling through distilled water heated at 81.7 °C[30]. For each compound, at least 3 samples were measured. The chemical compatibility of REPO₄ with conventional silicon bond coat was evaluated by identifying phase compositions of REPO₄ and Si powder mixtures with a weight ratio 7:3 after dwelling at 1,350 °C in air for 20 h.

Results

Crystal structure, phase compositions and densities of REPO₄ (RE = Lu, Yb, Er, Y and Sc). Figure 1 shows the typical crystal structure of Xenotime-type rare earth phosphate REPO₄. As shown, REPO₄ exhibits a tetragonal structure consisting of two types of polyhedra, i.e. PO₄ tetrahedra and REO₈ dodecahedra. In addition, the REPO₄ crystals can be considered as the accumulation of vertex-connected PO₄ tetrahedra and REO₈ dodecahedra. In PO₄ tetrahedra, the P atom is surrounded by four O atoms; whereas, in REO₈ polyhedra, the RE atom is surrounded by eight O atoms. As shown in Fig. 1b, each oxygen atom connects two RE atoms and one P atom; whereas, each RE atom or P atom solely connects oxygen atoms, with the former connected to eight oxygen atoms and latter four respectively.

Figure 2 shows the XRD patterns of sintered REPO₄ (RE = Lu, Yb, Er, Y and Sc) ceramic bulks. The measured patterns of REPO₄ are compared with the standard XRD spectra of LuPO₄ (ICDD PDF No. 43-0003), suggesting that single REPO₄ phases have been formed. With an increase of ionic radius of rare earth element (from Sc to Y), the diffraction peaks are expected, according to the Bragger's law, to shift to lower angle. It is worth pointing out that, whereas the cationic sizes of Lu³⁺, Yb³⁺, Er³⁺, Y³⁺ are more or less in the same order, the ionic size of Sc³⁺ is considerably smaller than that of the above four cations. As a result, ScPO₄ shows an XRD pattern dramatically shifted to higher 2θ angles, which is distinctive from the XRD patterns of the other four rare earth phosphates. Table 1 shows the measured, theoretical and relative densities of REPO₄ (RE = Lu, Yb, Er, Y and Sc). As shown, the sintered pellets have achieved a high relative density, more than 97% of theoretical density.

The predicted elastic constants of REPO₄ (RE = Lu, Yb, Er, Y and Sc) from first principles calculations. Table 2 shows the predicted elastic constants of REPO₄ (RE = Lu, Yb, Er, Y and Sc) from first-principle calculations. As shown, no negative C_{ij} value is obtained for these compounds, suggesting that these crystal structures are all stable. For those tetragonal structures such as the current Xenotime-type rare earth phosphates, $C_{22} = C_{11}$ and $C_{55} = C_{11}$. As shown in Table 2, the values of C_{11} and C_{22} are lower than those of C_{33}, indicating that the chemical bonds are identical in the directions of [100] and [010] but they are weaker than those in the [001]
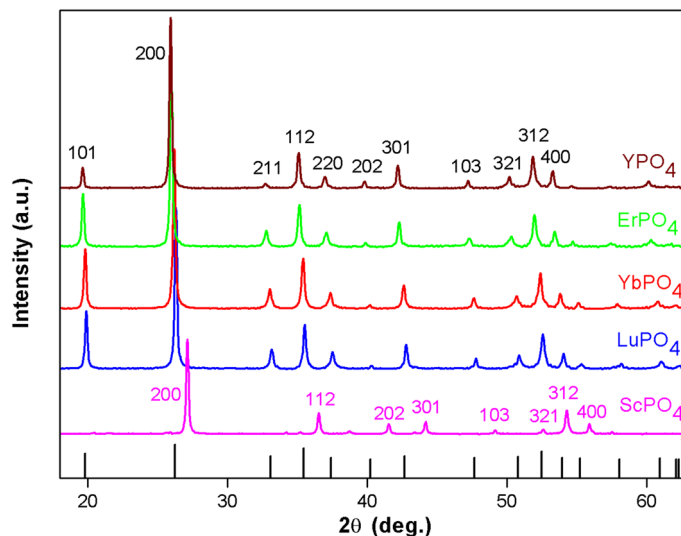
Figure 2. XRD patterns of sintered $REPO_4$ ceramic bulks ($RE = Lu$, Yb, Er, Y and Sc). $ScPO_4$ shows a pattern dramatically shifted to higher 2θ angles, attributing to a much smaller cationic size of Sc^{4+} than the other four rare earth elements.

Compound	$ScPO_4$	YPO_4	$ErPO_4$	$YbPO_4$	$LuPO_4$
Experimental density (g/cm^3)	3.78	4.38	6.05	6.95	6.02
Theoretical density (g/cm^3)	3.89	4.48	6.20	7.10	6.17
Relative density (%)	97.2	97.7	97.6	97.9	97.5

Table 1. The measured, theoretical and relative density of $REPO_4$ ($RE = Lu$, Yb, Er, Y and Sc).

Compound	$ScPO_4$	YPO_4	$ErPO_4$	$YbPO_4$	$LuPO_4$
C_{11}	285.9	399.2	265.7	245.7	326.9
C_{12}	22.1	18.5	28.8	26.1	32.6
C_{13}	89.5	80.2	96.3	81.0	111.0
C_{22}	285.9	399.2	265.7	245.7	326.9
C_{33}	300.0	407.7	367.1	326.5	403.8
C_{44}	93.6	71.3	78.5	68.3	80.4
C_{55}	285.9	399.2	265.7	245.7	326.9
C_{66}	41.9	32.8	22.5	19.8	31.9

Table 2. Elastic constants C_{ij} (in GPa) of $REPO_4$ ($RE = Lu$, Yb, Er, Y and Sc) from first principles calculations.

direction for current studied $REPO_4$ compounds. In fact, both RE–O and P–O bonds in Xenotime-type $REPO_4$ crystal structures can be divided into two groups, which are longer and shorter bonds respectively. Understandably, those shorter RE–O and P–O bonds tend to generate a stronger covalent character than those longer ones[31]. Referring to the crystal structure of $REPO_4$, the shorter bonds are aligned mainly along the [001] direction. As a result, the calculated C_{33} values are larger than those of C_{11} and C_{22}.

For the pure shear C_{ij} constants, the present calculations show that, for all $REPO_4$ structures currently investigated, C_{55} and C_{44} are significantly larger than C_{66}, suggesting that there are probably soft P-O and RE–O bonds on the (001) plane but rigid P-O and RE–O bonds on the (001) and (010) planes[32]. It further indicates shear deformation is easier to take place on the (001) plane. For the other non-diagonal elastic constants, their values are relatively small. The off-diagonal elements also reflect the deviation of atomic force constants from those of central type[33]. For the crystal dominated by central forces, Cauchy's relation implies that $C_{12} = C_{66}$, $C_{13} = C_{55}$, $C_{23} = C_{44}$ and $C_{25} = C_{46}$. Applying these conditions to $REPO_4$ compounds, they exhibit weak many-body forces such as angular and torsional interactions. To sum up above discussions, for Xenotime-type $REPO_4$ compounds, tensile and compressive deformation takes place primarily along the [100] and [010] directions whilst shear deformation takes place primarily on the (001) plane.
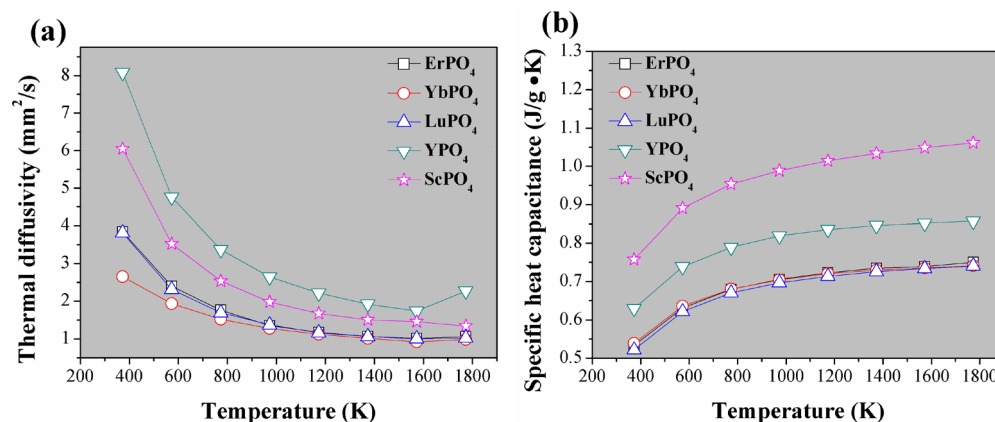
Figure 3. The measured thermal diffusivity (**a**) and calculated specific heat capacitance (**b**) of REPO$_4$ (RE = Lu, Yb, Er, Y and Sc) according to Neumann–Kopp rule.
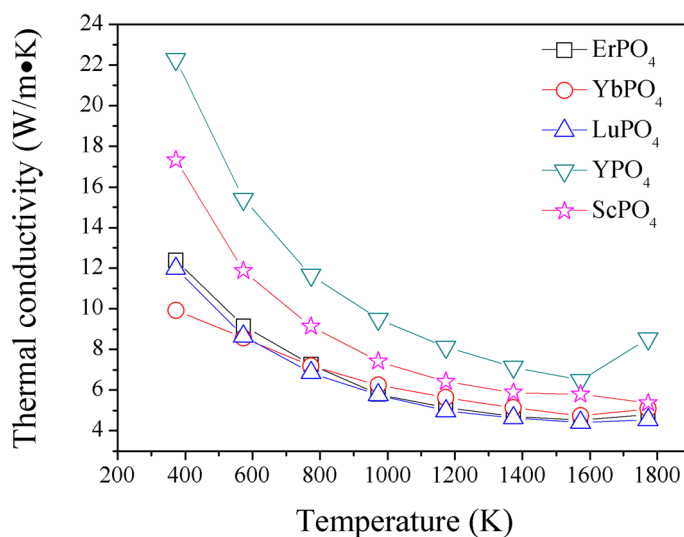

Figure 4. The measured thermal conductivity of REPO$_4$ (RE = Lu, Yb, Er, Y and Sc).

The measured thermophysical properties of REPO$_4$ (RE = Lu, Yb, Er, Y and Sc). *Thermal diffusivity/ conductivity of REPO$_4$ (RE = Lu, Yb, Er, Y and Sc).* Figure 3 shows the thermal diffusivity (a) and calculated specific heat capacitance (b) of REPO$_4$. As shown, rare earth phosphates REPO$_4$ exhibit thermal diffusivities lower than 3 mm^2/s from 1,200 K to 1773 K. By using density values (Table 1) and thermal diffusivity and specific heat capacitance shown in Fig. 3b, thermal conductivities of REPO$_4$ can be calculated according to Eq. (1), and are shown in Fig. 4. From it, the following trends can be found. First, the thermal conductivities of REPO$_4$ are generally decreasing with an increase of temperature. This is a typical feature for a ceramic whose heat transport is dictated by the phonon–phonon Umklapp scattering. Second, a heavier rare earth element of REPO$_4$, for instance, RE = Er, Yb, Lu, tends to generate lower thermal conductivity than those of lighter rare earth elements. Indeed, these three REPO$_4$ compounds with heavier rare earth elements have almost overlapping thermal conductivity- temperature curves, i.e. very similar thermal conductivity values.

Thermal expansion coefficient of REPO$_4$ (RE = Lu, Yb, Er, Y and Sc). Figure 5 exhibits the measured thermal expansion coefficients of REPO$_4$ (RE = Lu, Yb, Er, Y and Sc) ceramic bulks. As a comparison, the TECs of typical SiC-based CMCs[4], Yb$_2$Si$_2$O$_7$ and Yb$_2$SiO$_5$[34], representatives of third generation EBC topcoat materials, are also included. As shown, the TECs of REPO$_4$ are rather close to those of Yb$_2$Si$_2$O$_7$, a compound that is thought to have good TEC matching with SiC based CMCs, suggesting that REPO$_4$ currently investigated probably has a good TEC matching with SiC based CMCs.
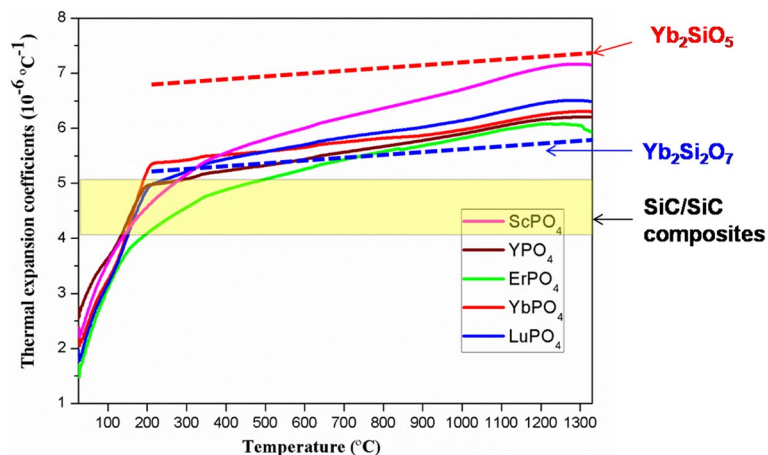
Figure 5. The measured thermal expansion coefficients of REPO$_4$ (RE = Lu, Yb, Er, Y and Sc). As a comparison, TEC of typical SiC-based CMCs (the horizontal bands)[4], TECs of Yb$_2$Si$_2$O$_7$ and Yb$_2$SiO$_5$[34] (the dashed lines) are also included.

Discussions

From the perspective of potential EBC applications, the following three aspects have to be taken into accounts. Firstly, from the mechanical aspect, a smaller elastic modulus together with a quasi-ductile behavior of an EBC topcoat material tends to produce a longer lifespan of its made coatings. From the elastic constants as unveiled in "The predicted elastic constants of REPO$_4$ (RE = Lu, Yb, Er, Y and Sc) from first principles calculations" section, different kinds of modulus (or mechanical parameters) can be calculated, such as bulk (*B*), shear (*G*), elastic (*E*) modulus respectively, as well as Poisson's ratio, *B*/*G* ratio, the latter two of which usually hints the extent of ductility of a material. Secondly, the thermophysical properties of EBC topcoat are usually of prior concern. The preliminary results in "The measured thermophysical properties of REPO$_4$ (RE = Lu, Yb, Er, Y and Sc)" section suggests a heavy rare earth element of REPO$_4$ tends to generate lower thermal conductivity, whilst a smaller rare earth element of REPO$_4$ (i.e. ScPO$_4$) tends to have a higher TEC. The underlying mechanisms need further investigation. Last but not least, the water vapor resistance, the thermochemical compatibility issues of REPO$_4$ have to be examined and justified as a potential EBC topcoat candidate. The following parts are to be discussed from the above three aspects.

Mechanical properties of REPO$_4$ (RE = Lu, Yb, Er, Y and Sc). As shown in Table 2, the elastic constants C_{ij} can be obtained from first principle calculations. In fact, REPO$_4$ has 13 independent elastic constants, i.e., C_{11}, C_{22}, C_{33}, C_{44}, C_{55}, C_{66}, C_{12}, C_{13}, C_{23}, C_{15}, C_{25}, C_{35} and C_{46}. Based on these elastic constants, the bulk modulus *B*, shear modulus *G* and Young's modulus *E* of REPO$_4$ can be further calculated. According to Voigt approximations[35–37], the bulk and shear moduli can be calculated from elastic constants as:

$$B_V = \frac{1}{9}(C_{11} + C_{22} + C_{33}) + \frac{2}{9}(C_{12} + C_{13} + C_{23}, \tag{2}$$

and

$$G_V = \frac{1}{15}(C_{11} + C_{22} + C_{33} - C_{12} - C_{13} - C_{23}) + \frac{2}{5}(C_{44} + C_{55} + C_{66}; \tag{3}$$

By contrast, on the basis of Reuss approximation, the bulk and shear moduli can be calculated from compliance matrix components as:

$$B_R = \frac{1}{(s_{11} + s_{22} + s_{33}) + 2(s_{12} + s_{13} + s_{23})}, \tag{4}$$

and

$$G_R = \frac{1}{4(s_{11} + s_{22} + s_{33} - s_{12} - s_{13} - s_{23}) + 3(s_{44} + s_{55} + s_{66})}, \tag{5}$$

where S_{ij} refers to the components of the elastic compliances that can be obtained through the inversion of the elastic constants ($S_{ij} = C_{ij}^{-1}$) tensor. Both the Voigt and Reuss averaging methods assume that strains and stresses are continuous in polycrystals and can produce respectively the upper and lower bounds of the effective bulk and shear moduli for polycrystals. On the contrary, the Voigt–Reuss–Hill (VRH) approach combines the upper and lower bounds, assuming that the average Voigt and Reuss elastic moduli are a good approximation of the macroscopic elastic moduli. The bulk modulus B_{VRH} and shear modulus G_{VRH} based on Voigt–Reuss–Hill approximation can be calculated as follows:

Compound	ScPO$_4$	YPO$_4$	ErPO$_4$	YbPO$_4$	LuPO$_4$
B	140.2	173.2	144.1	129.3	170.4
B^{exp}	203 ± 7[40]	186 ± 5[40]	168 ± 4[32]	150 ± 5[41]	169.3[38]
G	84.4	87.2	68.8	61.8	80.9
E	210.8	224.1	178.1	160.0	209.6
v	0.25	0.28	0.29	0.29	0.29
B/G	1.66	1.99	2.09	2.09	2.11

Table 3. Elastic moduli B, G, and E (in GPa), Poisson's ratio v, B/G ratio, and Vickers hardness H_V (in GPa) in the Hill approximation. Experimental bulk modii are included as a comparison.
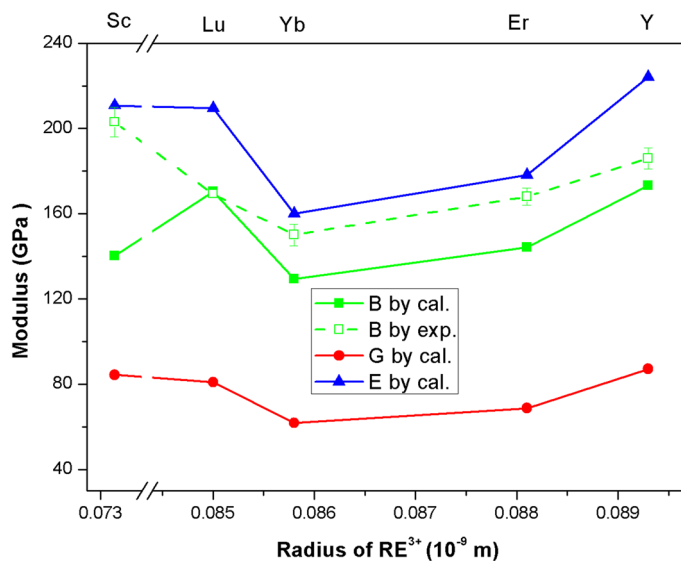

Figure 6. The plot of calculated bulk (B), shear (G) and Young's (E) moduli of REPO$_4$ versus cationic radius of RE^{3+}.

$$B_{VRH} = \frac{1}{2}(B_V + B_R), \tag{6}$$

$$G_{VRH} = \frac{1}{2}(G_V + G_R). \tag{7}$$

In the following context, we employ B_{VRH} and G_{VRH} as the calculated bulk modulus and shear modulus. In addition, according to Ref.[38], the Young's modulus E and Poisson's ratio v can be calculated on the basis of B_{VRH} and G_{VRH}[39] as follows:

$$E = \frac{9B_{VRH}G_{VRH}}{3B_{VRH} + G_{VRH}}, \tag{8}$$

$$v = \frac{3B_{VRH} - 2G_{VRH}}{2(3B_{VRH} + G_{VRH})}. \tag{9}$$

Table 3 shows the calculated bulk modulus B, shear modulus G, and Young's modulus E, Poisson's ratio v, and B/G ratio. As a comparison, the measured bulk moduli of rare earth phosphates are also included. Figure 6 plots the variation of bulk, shear and Young's modulus of REPO$_4$ versus the radius of rare earth elements. From it, the following trends can be found. Firstly, with an increase of ionic radius of rare earth element RE^{3+}, except for the calculated bulk modulus of ScPO$_4$, the calculated Young's, bulk and shear modulus decreases till Yb, and then increases. In other words, YbPO$_4$ is predicted to have the lowest above three moduli. Interestingly, this trend is perfectly conforming to the measured bulk modulus from other work[32,38,40,41] as shown the dash curve in Fig. 6, which confirms the validity of current calculation. The only discrepancy lies in that a much lower bulk modulus of ScPO$_4$ is predicted compared to the measured value.

In addition, if we closely examine the Poisson's ratio and B/G ratio, we can find rare earth phosphates REPO$_4$ are rather ductile and even show some plastic deformation that is rare for ceramics, which is desirable for EBC
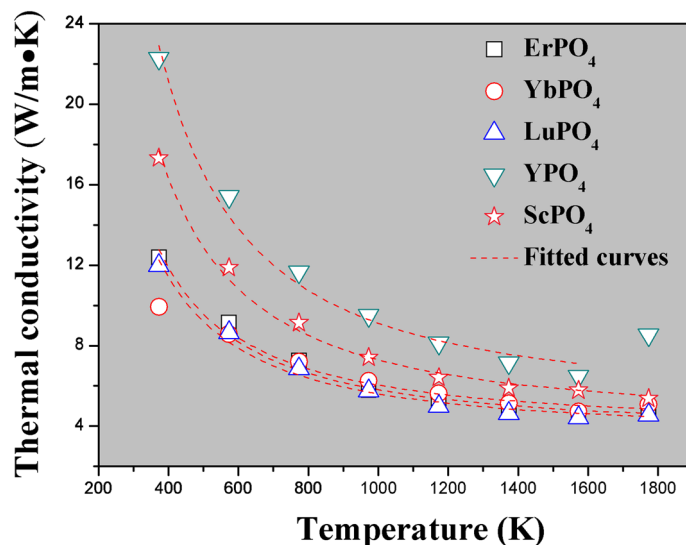
Figure 7. The fitted curves of thermal conductivity versus temperature according to Eq. (10) for REPO$_4$ (RE = Er, Yb, Lu, Y, Sc).

application. As we know, the Poisson's ratio reflects the capability of a material to resist deformation in different directions, and a greater Poisson's ratio usually yields a better plasticity and ductility of a material[42]. For instance, the Poisson's ratio of metals is usually greater than 0.3. By contrast, the Poisson's ratio of ceramics is usually below 0.3. For example, the Poisson's ratios of zirconia (ZrO$_2$), lanthanum zirconate (La$_2$Zr$_2$O$_7$) and alumina are 0.27, 0.25 and 0.23 respectively. Except for ScPO$_4$, the Possion's ratios of the other rare earth phosphate currently investigated are in the range of 0.28–0.29, which is comparable to most intermetallic compounds. This suggests REPO$_4$ are relatively plastic and ductile.

Furthermore, the B/G value further supports the above conclusion. The B/G value can be taken as a criterion to distinguish a material whether it has a good ductility or not. In general, materials with a B/G value below 1.75 tend to have poor ductility, whereas, materials with a B/G value above 2.0 tend to have excellent ductility. The B/G values of REPO$_4$ except ScPO$_4$ are in a range of 1.99–2.11, which lies in the plastic and ductile region. The Poisson's ratio and B/G value of ScPO$_4$ are 0.25 and 1.66 respectively, indicating that it might possess a typical feature of ceramic brittleness. As a comparison, the Poisson's ratio and B/G value of RE$_2$SiO$_5$ are in the range of 0.20–0.25 and 1.46–1.73 respectively[43], which are lower than values of REPO$_4$, suggesting they exhibit a more brittle nature than currently investigated REPO$_4$. By contrast, the Poisson's ratio and B/G value of RE$_2$Si$_2$O$_7$ are in the range of 0.30–0.31 and 2.33–2.35[44] respectively, suggesting that RE$_2$Si$_2$O$_7$ might possess even better behavior than REPO$_4$ in terms of toughness. In fact, it is worth pointing out that, due to such quasi-ductile behavior of RE$_2$Si$_2$O$_7$ and REPO$_4$, they have been proposed as a novel interphase candidate for SiC/SiC interphase so as to improve oxidation resistance of interphase[8,9], replacing conventional layered PyC or BN which are highly susceptible to oxidation at low temperatures.

To sum up, in terms of modulus, YbPO$_4$ exhibits lowest value, which perhaps suggests it might provide best strain tolerance of its made coating and is thus desirable for EBC topcoat application. Meanwhile, from quasi-ductile perspective, ErPO$_4$, YbPO$_4$ and LuPO$_4$ exhibit excellent behavior, suggesting they might produce durable coatings.

Thermophysical properties of REPO$_4$ (RE = Lu, Yb, Er, Y and Sc). According to[45–47], the Grüneisen parameter γ, which is a reflection of lattice anharmonicity, is closely related to the thermophysical properties of a material, such as thermal conductivity and thermal expansion coefficient. Based on the formalism developed in[45], the Grüneisen parameter γ can be calculated according to the following equation:

$$\gamma = Ma\omega_D^3/(2664.8 \times A) \tag{10}$$

in which M, a, ω_D are average atomic mass, size in the lattice and Debye characteristic frequency respectively, while A is a parameter that can be obtained by curve fitting of thermal conductivity (k) versus temperature (T) curves (refer to Fig. 7) according to Eq. (11):

$$k = \frac{A}{3T_1} + \frac{2A\sqrt{T_1}}{3T^{1.5}}, \tag{11}$$

where A and T$_1$ are characteristic parameters. In fact, Eq. (11) depicts the thermal conductivity of a lattice without any point defects, where phonon–phonon Umklapp scattering is the dictating factor to define its thermal conductivity. In fact, according to[45,46], A/3T$_1$ in Eq. (11) represents the minimal lattice thermal conductivity, k_{min}, neglecting thermal radiation effects, and can be further expressed as follows:

	M^a (10^{-26} kg)	a^{3b} (10^{-29} m³)	a^b (Å)	ρ^b ($\times 10^3$ kg/m³)	ν^c (m/s)	ω_D ($\times 10^{13}$ Hz)^d	θ_D (K)^e	A (W/m)^f	T_1 (K)^f	γ^g	$k_{min}{}^h$
LuPO₄	7.471	1.211	2.296	6.17	4,643	7.882	601.9	4,563.4 ± 101.5	420.2 ± 28.1	0.69	3.62
YbPO₄	7.417	1.044	2.186	7.10	3,883	6.924	528.7	4,882.1 ± 150.9	418.3 ± 29.8	0.41	3.89
ErPO₄	7.256	1.170	2.270	6.20	3,724	6.394	488.3	4,753.8 ± 136.5	427.7 ± 37.8	0.34	3.70
YPO₄	5.089	1.136	2.248	4.48	5,785	10.031	766.0	8,264.7 ± 173.6	545.2 ± 45.8	0.52	5.05
ScPO₄	3.873	0.996	2.151	3.89	6,025	10.918	833.7	6,444.2 ± 92.7	507.5 ± 24.5	0.63	4.23

Table 4. Some basic parameters of REPO₄ (RE = Lu, Yb, Er, Y, Sc). [a]Average atomic mass in REPO₄ lattice; [b]Average atomic volume in the REPO₄ lattice, can be calculated as: $a^3 = M/\rho$, in which ρ is theoretical density of each compound; a is average atomic size; [c]Sound speed. $\nu = \frac{1}{3}(\frac{2}{v_t^3} + \frac{1}{v_t^3})^{-1/3}$, while $v_l = \sqrt{(B + \frac{4}{3}G)/\rho}$; $v_t = \sqrt{G/\rho}$ [22], where B and G are bulk modulus and shear modulus respectively, and are used values in Table 3; [d]Debye frequency, is calculated according to $\omega_D = (6\pi^2)^{1/3} \nu/a$ [45]; [e]Debye temperature, is calculated according to $\theta_D = \hbar\omega_D/k_B$; in which $\hbar$ and k_B are Planck constant and Boltzmann constant respectively; [f]Are fitted values from curve fitting in Fig. 7; [g]Grüneisen parameters, representing lattice anharmonicity, is calculated according to: $\gamma = Ma\omega_D^3/(2,664.8 \times A)$; [h]$k_{min} = A/3T_1$.
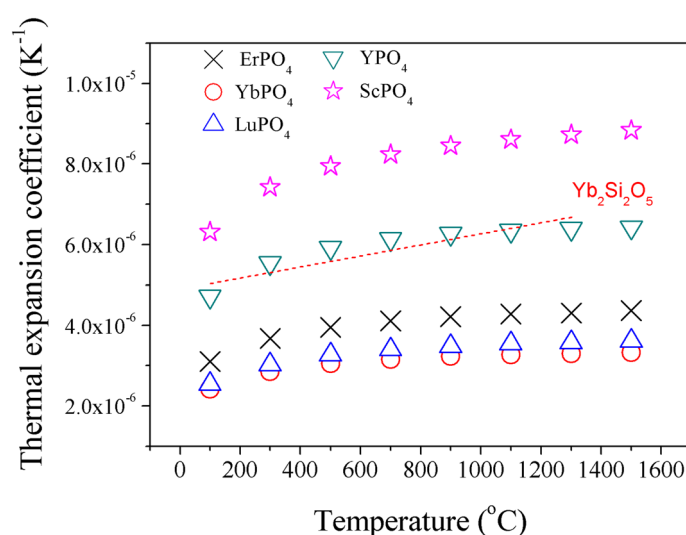

Figure 8. The calculated TEC of REPO₄ according to Eq. (12) on the basis of measured specific heat capacitance (refer to Fig. 3b). As a reference, the measured TECs of Yb₂Si₂O₇[34] have also been included.

$$k_{min} = \frac{A}{3T_1} = \xi\sqrt{\frac{E}{aM\gamma}}, \tag{12}$$

where ξ is a constant. From Eq. (12), it is apparent that, a material with higher average atomic mass (i.e. bigger M) and stronger lattice anharmonicity (i.e. larger γ values) tends to generate lower thermal conductivity. This perhaps explains ErPO₄, YbPO₄ and LuPO₄ have lower thermal conductivities than YPO₄, ScPO₄, as Er, Yb and Lu have much heavier atomic mass than Y and Sc.

Table 4 shows some basic parameters of REPO₄ and the related calculation method of each parameter has been attached under the table. As shown, from the fitting of k-T curves (which yields A and T_1) and the calculation of other related physic parameters, the Grüneisen parameters can be obtained according to Eq. (10). It is found that, the currently studied rare earth phosphates all exhibit very small Grüneisen parameters.

In fact, the thermal expansion coefficient α of a material has the following relationship with Grüneisen parameter[48]:

$$\alpha = c_P \rho \gamma / 3B \tag{13}$$

where c_P is specific heat capacitance (in J/g K), ρ is density (in g/cm³), B is the bulk modulus (in GPa) and γ is the Grüneisen parameter. On the basis of Eq. (13), by employing the measured c_P values (Fig. 3b), we can calculate thermal expansion coefficients of REPO₄ (Fig. 8), by using ρ, γ values from Table 4 and B values from Table 3.

As shown in Fig. 8, the calculated TECs are rather close to those measured ones (refer to Fig. 5) which are in principle lying between curves of Yb₂SiO₅ and Yb₂Si₂O₇, suggesting the validity of the current methodology. It is worth pointing out that both measured and calculated TEC values indicate ScPO₄ has highest value whilst those rare earth phosphates REPO₄ with heavier atomic mass have lower values. The discrepancy of these calculated and
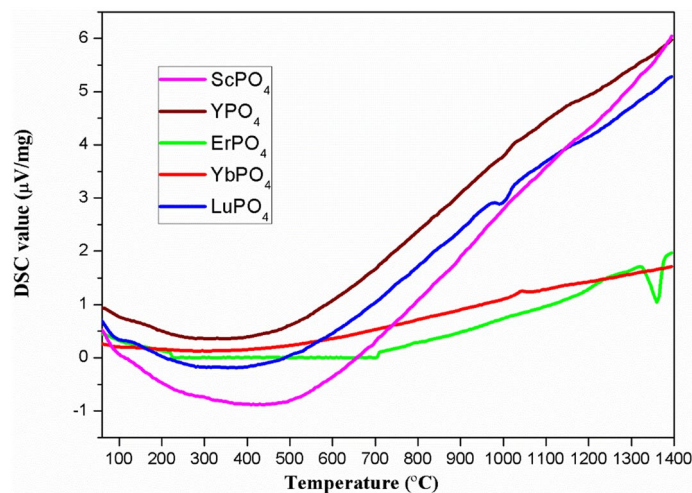
Figure 9. The DSC curves of REPO4 powders (RE = Lu, Yb, Er, Y and Sc).

Compound	ScPO$_4$	YPO$_4$	ErPO$_4$	YbPO$_4$	LuPO$_4$	Yb$_2$SiO$_5$	Yb$_2$Si$_2$O$_7$
Corrosion rate constants ($\times 10^{-4}$ mg/ cm^2 h)	2.32 ± 0.91	2.51 ± 1.33	4.08 ± 1.87	4.31 ± 1.92	1.89 ± 1.03	7.46 ± 3.24	11.02 ± 3.91

Table 5. Comparison of corrosion rate constants of REPO$_4$ (RE = Lu, Yb, Er, Y and Sc). As a comparison, the values of Yb$_2$SiO$_5$ and Yb$_2$Si$_2$O$_7$ are also included. The normalized conditions are 50% H$_2$O-balance O$_2$ vapor with a flow of 0.3 cm/s and a total pressure of 1 atm at 1,500 °C for 80 h.

measured TEC values might originate from the slight temperature dependence of density ρ and bulk modulus B, which is neglected in current calculations.

By comparing Eqs. (12) and (13), it is again affirmed that the Grüneisen parameter γ has an important role in determining both thermal conductivity k and thermal expansion coefficient α. In addition, the modulus, which is a reflection of bond strength, is another parameter affecting both k and α. Different from thermal barrier coating application, which requires a topcoat material desirably having lower k and higher α, EBC topcoat material needs to have lower k but lower α, as a result of relatively low TEC of common SiC based CMCs (refer to Fig. 5). According to Eqs. (12) and (13), theoretically a low thermal conductivity and high thermal expansion (which is desirable for TBC application) can be achieved simultaneously. However, unfortunately, a low thermal conductivity and low thermal expansion coefficient are exclusive, and thus cannot be achieved simultaneously. This suggests that, for the selection of EBC topcoat material, a compromise of k and α (or, a compromise of lattice anharmonicity and bond strength) would be recommended, which is distinctive from the selection of TBC topcoat material where materials with strong lattice anharmonicity and weak bonding are favored.

The justification of REPO$_4$ (RE = Lu, Yb, Er, Y and Sc) for potential EBC topcoat application.
Except the mechanical and thermophysical properties, the high temperature stability, the CMAS resistance, as well as water vapor resistance of a candidate EBC topcoat are also important factors. Hence, we discuss these properties of xenotime-type REPO$_4$ (RE = Lu, Yb, Er, Y and Sc) as follows.

As discussed in[21–23], rare earth phosphates exhibit excellent CMAS resistance, attributed to a dense and crack-free layer formed on the surface of REPO$_4$ as a result of their reaction with molten CMAS. These dense layers suppress the further penetration of CMAS melts[23]. In addition, the xenotime-type REPO$_4$ (RE = Lu, Yb, Er, Y and Sc) exhibits very good high-temperature stability, as shown in Fig. 9, which illustrates the DSC curves of current investigated rare earth phosphates measured in ambient atmosphere up to 1,400 °C. As shown, there are no endothermic or exothermic peaks detected for REPO$_4$ (RE = Lu, Yb, Y and Sc), suggesting they have very good phase stability up to 1,400 °C. However, for ErPO$_4$, there is a peak around 1,350 °C, suggesting that there might be a phase transformation around this temperature.

As a potential EBC topcoat material, the water vapor corrosion resistance is a key factor. Table 5 exhibits the water vapor corrosion rates of REPO$_4$ at a normalized condition of 50% H$_2$O-balance O$_2$ vapor with a flow of 0.3 cm/s and a total pressure of 1 atm at 1,500 °C for 80 h. For comparison, the values of Yb$_2$SiO$_5$ and Yb$_2$Si$_2$O$_7$ are also included. As shown, the current investigated REPO$_4$ has better water vapor corrosion resistance compared to third generation rare earth silicates.

Regarding the data shown in Table 5, there is a concern raised from the execution of high temperature water vapor test by use of an alumina tube furnace. Unfortunately, a reaction product Al$_5$RE$_3$O$_{12}$ has been found on the surface of bulk samples after high temperature water vapor corrosion test. The formation mechanism of byproduct Al$_5$RE$_3$O$_{12}$ is likely to be two steps as shown in the Chemical Formula (R1) and (R2). Firstly, the solid

	Weight of 3 molar REPO$_4$ (g)	Weight gain (g)	Weigh gain percentage relative to REPO$_4$ mass (%)
LuPO$_4$	810	42	5.2
YbPO$_4$	804	42	5.2
ErPO$_4$	787	42	5.3
YPO$_4$	551.7	42	7.6
ScPO$_4$	420	42	10

Table 6. The weight gain and weight gain percentage relative to original REPO$_4$ mass, assuming a thorough reaction according to Chemical Formula (R3), i.e. all REPO$_4$ has been consumed by Al$_2$O$_3$.
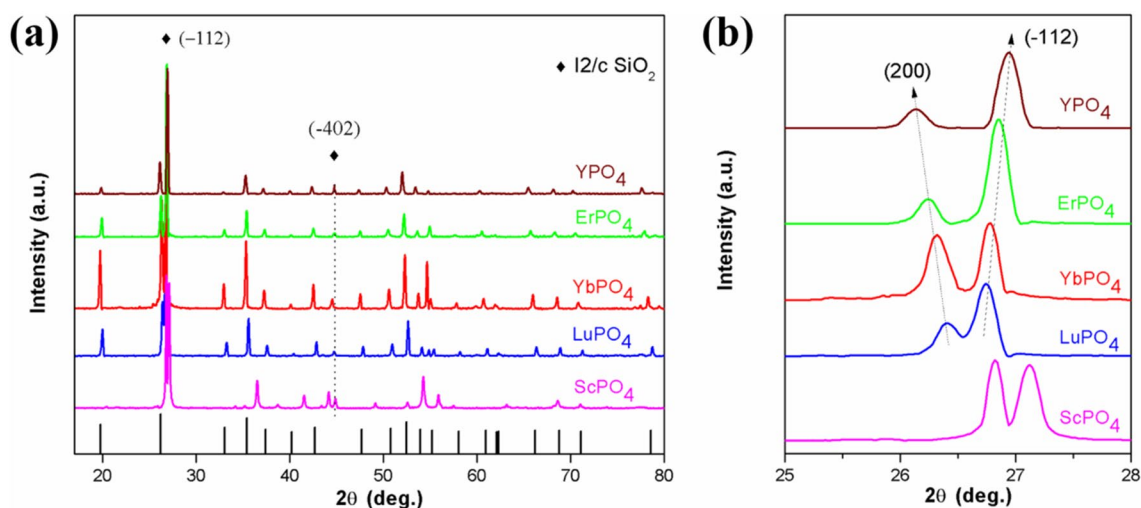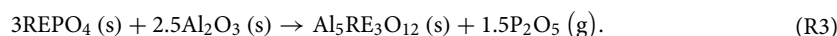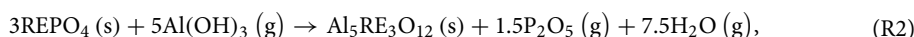

Figure 10. XRD patterns of REPO$_4$ mixed with silicon after heat treatment at 1,350 °C for 20 h: (a) $17° \leq 2\theta \leq 80°$; (b) $25° \leq 2\theta \leq 28°$.

Al$_2$O$_3$ from alumina tube reacts with water vapor to form gaseous Al(OH)$_3$. Secondly, the gaseous Al(OH)$_3$ then reacts with REPO$_4$ to form solid Al$_5$RE$_3$O$_{12}$. By combining Chemical Formula (R1) and (R2), we then can reach Chemical Formula (R3).

$$2.5 \, Al_2O_3 \, (s) + 7.5H_2O \, (g) \rightarrow 5Al(OH)_3 \, (g), \tag{R1}$$

$$3REPO_4 \, (s) + 5Al(OH)_3 \, (g) \rightarrow Al_5RE_3O_{12} \, (s) + 1.5P_2O_5 \, (g) + 7.5H_2O \, (g), \tag{R2}$$

$$3REPO_4 \, (s) + 2.5Al_2O_3 \, (s) \rightarrow Al_5RE_3O_{12} \, (s) + 1.5P_2O_5 \, (g). \tag{R3}$$

As these chemical reactions would probably affects weight loss or gain during water vapor corrosion test of REPO$_4$ bulk samples, we would firstly evaluate the potential effect on weight change of these reactions. According to Chemical Formula (R3), the ingest of alumina from the environment will lead to weight gain, whilst the formation of gaseous product P$_2$O$_5$ will cause weight loss. Hence, the weight change is dependent on these two factors. As the weight of 2.5 molar ingested Al$_2$O$_3$ is slightly higher than that of 1.5 molar gaseous P$_2$O$_5$, this reaction would result in a gentle increase of weight. According to Chemical Formula (R3), the reaction of 3 molar REPO$_4$ will lead to a weight gain of 42 g. Table 6 shows weight gain percentage relative to the REPO$_4$ mass according to a thorough reaction conforming to Formula (R3), i.e. all REPO$_4$ has been consumed by alumina. As shown, given all REPO$_4$ has been consumed to form Al$_5$RE$_3$O$_{12}$, only a 5–10% weight gain would be generated. However, in reality, only a small amount of REPO$_4$ reacts with Al$_2$O$_3$ from the alumina tube to form Al$_5$RE$_3$O$_{12}$. Hence, a negligible weight gain, at least smaller than the error bar, would be generated due to the above byproduct formation. Therefore, the current obtained water vapor resistance data are still reliable.

Finally, the chemical compatibility between REPO$_4$ (RE = Lu, Yb, Er, Y and Sc) and Si bond layer is further investigated. After annealing of 30 wt.% silicon and REPO$_4$ powders at 1,350 °C for 20 h, the powder mixtures are then subject to x-ray diffraction and their patterns are shown in Fig. 10. As shown, the characteristic peaks of Moganite-type SiO$_2$, as indicated in Fig. 10a, have been present. In Fig. 10b, which is a high magnitude XRD pattern of $25° \leq 2\theta \leq 28°$, the XRD peaks of Xenotime-type REPO$_4$ denoting (2 0 0) planes are systematically shifting towards lower 2θ angles with an increase of cationic radius of RE, which is consistent with Bragg's law. By contrast, the peak positions of (-1 1 2) planes of Moganite-type SiO$_2$ keep relatively unchanged. There are no

impurity peaks except the above two phases, suggesting that the current investigated REPO$_4$ is thermochemically compatible with the silicon bond coat.

Conclusion

The mechanical and thermophysical properties of Xenotime-type REPO$_4$ (RE = Lu, Yb, Er, Y and Sc) have been thoroughly investigated by first-principle calculations and experimental studies respectively with a potential environmental barrier coating application. The main conclusions are as follows. First, from calculations, large Poisson's ratio and big B/G ratio are predicted for currently investigated rare earth phosphate compounds except ScPO$_4$, suggesting that they have some sort of quasi-ductile behavior, which is perhaps beneficial to the durability and lifespan of their made coatings. Second, from the study of underlying parameters governing thermophysical properties of a ceramic, it suggests that, a low thermal expansion coefficient (which yields a good TEC matching of EBC with SiC-based CMC substrates) and a low thermal conductivity (which provides perhaps a good thermal insulation of EBC) are unfortunately exclusive, and thus not possible to achieve simultaneously. For EBC application, a good TEC match of topcoats and substrates is perhaps more important than thermal insulation properties, suggesting a weak lattice anharmonicity of a lattice might be beneficial. However, a weak lattice anharmonicity, i.e. strong lattice harmonicity might result in strong bonds, i.e. larger elastic modulus, which might be detrimental to the strain tolerance of its coatings. This suggests that a compromised value of TEC and thermal conductivities of a topcoat material is more favorable. In fact, the current studied REPO$_4$ exhibits a very good TEC match with SiC-based CMCs, particularly for those heavier rare earth elements. Third, the current investigated REPO$_4$ exhibits very good high-temperature water vapor corrosion resistance, excellent CMAS resistance as well as excellent chemical compatibility with silicon bond coats at elevated temperatures. By considering the above three aspects, it is proposed that Xenotime-type rare earth phosphates are a promising EBC topcoat material.

References

1. Padture, N. P. Advanced structural ceramics in aerospace propulsion. *Nat. Mater.* **15**, 804–809 (2016).
2. Lee, K. N., Fox, D. S. & Bansal, N. P. Rare earth silicate environmental barrier coatings for SiC/SiC composites and Si$_3$N$_4$ ceramics. *J. Eur. Ceram. Soc.* **25**, 1705–1715 (2005).
3. Clarke, D. R. & Phillpot, S. R. Thermal barrier coating materials. *Mater. Today* **8**, 22–29 (2005).
4. Turcer, L. R. & Padture, N. P. Towards multifunctional thermal environmental barrier coatings (TEBCs) based on rare-earth pyrosilicate solid-solution ceramics. *Scrip. Mater.* **154**, 111–117 (2018).
5. Richards, B. T. *et al.* Response of ytterbium disilicate-silicon environmental barrier coatings to thermal cycling in water vapor. *Acta Mater.* **106**, 1–14 (2016).
6. Richards, B. T. & Wadley, H. N. G. Plasma spray deposition of tri-layer environmental barrier coatings. *J. Eur. Ceram. Soc.* **34**, 3069–3083 (2014).
7. Padture, N. P. Environmental degradation of high-temperature protective coatings for ceramic-matrix composites in gas-turbine engines. *NPJ Mater. Deg.* **3**, 10–15 (2019).
8. Boakye, E. E. *et al.* Processing and testing of RE$_2$Si$_2$O$_7$ fiber-matrix interphase for SiC–SiC composites. *J. Am. Ceram. Soc.* **99**, 415–423 (2016).
9. Boakye, E. E. *et al.* In situ Y$_2$Si$_2$O$_7$ coatings on Hi-Nicalon-S SiC fibers: phase formation and fiber strength. *J. Am. Ceram. Soc.* **102**, 5725–5737 (2019).
10. Wang, P. *et al.* Oxidation behavior of SiC$_f$/SiC composites modified by layered-Y$_2$Si$_2$O$_7$ in wet oxygen environment. *J. Inorg. Mater.* **34**, 904–908 (2019).
11. Golden, R. A. & Opila, E. J. High-temperature oxidation of yttrium silicides. *J. Mater. Sci.* **53**, 3981–4000 (2018).
12. Anton, R., Leisner, V., Watermeyer, P., Engstler, M. & Schulz, U. Hafnia-doped silicon bond coats manufactured by PVD for SiC/SiC CMCs. *Acta Mater.* https://doi.org/10.1016/j.actamat.2019.10.050 (2019).
13. Harder, B. J. Oxidation performance of Si-HfO$_2$ Environmental barrier coating bond coats deposited via plasma-physical vapor deposition. *Surf. Coat. Technol.* https://doi.org/10.1016/j.surfcoat.2019.125311 (2019).
14. Robertson, A. L., Sola, F., Zhu, D., Salem, J. & White, K. W. Microscale fracture mechanisms of HfO$_2$-Si environmental barrier coatings. *J. Eur. Ceram. Soc.* **39**, 2409–2418 (2019).
15. Zhu, D. & Hurst, J.B. Advanced high temperature and fatigue resistant environmental barrier coating bond coat systems for SiC/SiC ceramic matrix composites, *U.S. Patent* 20130344319A1 (2013).
16. Poerschke, D. L., Shaw, J. H., Verma, N., Zok, F. W. & Levi, C. G. Interaction of yttrium disilicate environmental barrier coatings with calcium-magnesium-iron alumino-silicate melts. *Acta Mater.* **145**, 451–461 (2018).
17. Bansal, N. P. & Lamon, J. *Ceramic Matrix Composites: Materials, Modelling and Technology* (Wiley, New York, 2014).
18. Richards, B. T., Sehr, S., de Franqueville, F., Begley, M. R. & Wadley, H. N. G. Fracture mechanisms of ytterbium monosilicate environmental barrier coatings during cyclic exposure. *Acta Mater.* **103**, 448–460 (2016).
19. Poerschke, D. L., Van Sluytman, J. S., Wong, K. B. & Levi, C. G. Thermochemical compatibility of ytterbia-(hfania/silica) multilayers for environmental barrier coatings. *Acta Mater.* **61**, 6743–6755 (2013).
20. Lee, K. N. *et al.* Upper temperature limit of environmental barrier coatings based on mullite and BSAS. *J. Am. Ceram. Soc.* **86**, 1299–1306 (2003).
21. Hu, X. *et al.* Thermal properties and calcium-magnesium-alumina-silicate (CMAS) resistance of LuPO$_4$ as environmental barrier coatings. *J. Eur. Ceram. Soc.* https://doi.org/10.1016/j.jeurceramsoc.2019.11.018 (2019).
22. Feng, J., Xiao, B., Zhou, R. & Pan, W. Anisotropy in elasticity and thermal conductivity of monazite-type REPO$_4$ (RE = La, Ce, Nd, Sm, Eu and Gd) from first-principles calculations. *Acta Mater.* **61**, 7364–7383 (2013).
23. Wang, F., Guo, L., Wang, C. M. & Ye, F. X. Calcium-magnesium-alumina-silicate (CMAS) resistance characteristics of LnPO$_4$ (Ln = Nd, Sm, Gd) thermal barrier coatings. *J. Eur. Ceram. Soc.* **37**, 289–296 (2017).
24. Wang, Y., Chen, X., Wen, L., Cheng, L. & Zhang, L. Exploration of YPO$_4$ as a potential environmental barrier coatings. *Ceram. Int.* **36**, 755–759 (2010).
25. Segall, M. D. *et al.* First-principles simulation: ideas, illustrations and the CASTEP code. *J. Phys. Condens. Matter.* **14**, 2717 (2002).
26. Chadi, D. J. & Cohen, M. L. Special points in the Brillouin zone. *Phys. Rev. B* **8**, 5747–5753 (1973).
27. Ceperley, D. M. & Alder, B. J. Ground state of the electron gas by a stochastic method. *Phys. Rev. Lett.* **45**, 566–569 (1980).

28. Leitner, J., Chuchvalec, P., Sedmidubsky, D., Strejc, A. & Abrman, P. Estimation of heat capacities of solid mixed oxides. *Thermochim. Acta* **395**, 27–46 (2003).
29. Barin, I. *Thermochemical Data of Pure Substances* 3rd edn. (VCH, Weinheim, 1995).
30. Liu, J. et al. Polymer-derived yttrium silicate coatings on 2D C/SiC composites. *J. Eur. Ceram. Soc.* **33**, 433–439 (2013).
31. Li, H., Zhang, S., Zhou, S. & Cao, X. Bonding characteristics, thermal expansibility, and compressibility of RXO_4 (R = Rare earths, X = P, As) within Monazite and zircon structures. *Inorg. Chem.* **48**, 4542–4548 (2009).
32. Lacomba, R., Errandonea, D., Meng, Y. & Bettinelli, M. High-pressure stability and compressibility of APO_4 (A=La, Nd, Eu, Gd, Er, and Y) orthophosphates: an X-ray diffraction study using synchrotron radiation. *Phys. Rev. B* **81**, 064113 (2010).
33. Mohapatra, H. & Eckhardt, C. J. The elastic constants and related mechanical properties of the monoclinic polymorph of the carbamazepine molecular crystal. *J. Phys. Chem. B* **112**, 2293 (2008).
34. Han, J., Wang, Y., Liu, R. & Cao, Y. Thermal shock behavior of mixed ytterbium disilicates and ytterbium monosilicates composite environmental barrier coatings. *Surf. Coat. Technol.* **352**, 348–353 (2018).
35. M. Von, Lehrbuch der kristallphysik & Teubner, B.G. 1928.
36. Reuss, A. Berechnung der Fliessgrenze von Mischkristallen auf Grand der Plastizitatsbedingung fun Einkristalle, Z.ang.math. mech, 9 (1929).
37. Hill, R. W. The elastic behavior of a crystalline aggregate. *Proc. Phys. Soc.* **65**, 349 (1952).
38. Thomä, R., Wehrle, H. & Armbruster, A. Measurement of the elastic constants of $LuAsO_4$ and $LuPO_4$ by Brillouin scattering and determination of the Debye temperatures. *Physica Status Solidi* **24**, K71–K73 (1974).
39. Green, D. *An Introduction to the Mechanical Properties of Ceramics* (Cambridge University Press, Cambridge, 1998).
40. Zhang, F. X. et al. High-pressure phase transitions of $ScPO_4$ and YPO_4. *Phy. Rev. B* **80**, 184114 (2009).
41. Zhang, F. X. et al. Pressure-induced zircon-type to scheelite-type phase transitions in $YbPO_4$ and $LuPO_4$. *J. Sol. Sta. Chem.* **181**, 2633–2638 (2008).
42. Grimvall, G. *Thermophysical Properties of Materials* (Elsevier, Amsterdam, 1986).
43. Tian, Z. et al. Theoretical and experimental determination of the major thermo-mechanical properties of RE_2SiO_5(RE = Tb, Dy, Ho, Er, Tm, Yb, Lu, and Y) for environmental and thermal barrier coating applications. *J. Eur. Ceram. Soc.* **36**, 189–202 (2016).
44. Tian, Z., Zheng, L., Li, Z., Li, J. & Wang, J. Exploration of the low thermal conductivities of γ-$Y_2Si_2O_7$, β-$Y_2Si_2O_7$, β-$Yb_2Si_2O_7$, and β-$Lu_2Si_2O_7$ as novel environmental barrier coating candidates. *J. Eur. Ceram. Soc.* **36**, 2813–2823 (2016).
45. Wang, Y., Yang, F. & Xiao, P. Glass-like thermal conductivities in (La1-x1)2(Zr1-x2Yx2)2O7-x2 (x = x1 + x2, 0 ≤ x ≤ 1.0) solid solutions. *Acta Mater.* **60**, 7024–7033 (2012).
46. Wang, Y., Yang, F. & Xiao, P. Role and dertermining factor of substitutional defects on thermal conductivity: a study of La2(Zr1-xBx)2O7 (B = Hf, Ce, 0 ≤ x ≤ 0.5) pyrochlore solid solutions. *Acta Mater.* **68**, 106–115 (2014).
47. Wang, Y., Yang, F. & Xiao, P. Rattlers or oxygen vacancies: determinant of high temperature plateau thermal conductivity in doped pyrochlores. *Appl. Phys. Lett.* **102**, 141902 (2013).
48. Belomestnykh, V. N. The acoustical Grüneisen constants of solids. *Tech. Phys. Lett.* **30**, 91–93 (2004).

Acknowledgment

Author contributions

Y.W. conceived the idea, J.H. conducted the experiments and the calculations, Wang and Han wrote the text, J.H. drew Figs. 1, 2 and 6, 9, 10, Y.W. drew Figs. 3, 4, 5, 7 and 8, Y.W., R.L., F.W. reviewed the whole manuscript.

Competing interests

The authors declare no competing interests.

Additional information

Correspondence and requests for materials should be addressed to Y.W.

Reprints and permissions information is available at www.nature.com/reprints.

Publisher's note Springer Nature remains neutral with regard to jurisdictional claims in published maps and institutional affiliations.